MTLA 35 (2024) 102122

Contents lists available at ScienceDirect

Materialia

journal homepage: www.elsevier.com/locate/mtla

Full Length Article

Basal and prismatic slip in hafnium

Siyang Wang *, Di Wang

Department of Materials, Royal School of Mines, Imperial College London, London SW7 2AZ, United Kingdom

ARTICLE INFO

Keywords:
Hafnium
Deformation
Micromechanics
Slip
Dislocation

ABSTRACT

Metals with hexagonal crystal structure are found in many safety-critical applications, from titanium alloy fan blades in jet engines to magnesium alloys in the automotive industry. They also exist in nuclear reactors, for example hafnium alloy control rods whose structural integrity is critical to nuclear safety. However, mechanistic understanding of the micromechanical properties and deformation behaviour of Hf remains elusive. To aid in this understanding, we performed *in situ* scanning electron microscopy single crystal micropillar compression tests of a commercial Hf alloy, where the samples were aligned to activate ⟨*a*⟩ prismatic and ⟨*a*⟩ basal slip systems. We then employed transmission electron microscopy to examine the dislocation structure in the deformed pillars. These two slip systems exhibited distinctly different behaviour, where prismatic slip is planar and basal slip is wavy. Prismatic slip is the easiest deformation mode, while basal slip is at least twice as difficult. Generally, the characters of prismatic and basal slip in Hf show similarities to those in some other hexagonal metals such as Ti and Zr, except for the higher relative difficulty of basal slip. Our results provide fundamental knowledge and parameters that can be used for modelling degradation and predicting performance of Hf, and shed light on the general behaviour of basal and prismatic slip systems in low-*c*/*a*-ratio hexagonal metals.

Hafnium is a relatively rare element, often found in association with zirconium minerals and primarily obtained as a by-product of zirconium refinement [1]. It shares the hexagonal close packed (HCP) crystal structure with Zr at room temperature [2]. The two elements are vastly difficult to separate mainly because of their chemical similarity [3]. Yet for their distinct applications in the nuclear industry, it is crucially important to avoid the impurity of one in another. Zr alloys are extensively used as fuel cladding in nuclear reactors due to their low neutron absorption cross section [4]. Hf alloys, conversely, show very high neutron absorption cross section, and are therefore used as control rods [5,6] for modulation of chain reaction rate and prevention of criticality accident. The safety of the reactors therefore relies crucially on the mechanical stability of the Hf control rods.

By virtue of their anisotropic mechanical properties inherited from the hexagonal crystal structure, plastic deformation of HCP metals/alloys, such as Ti in jet engines, Zr and Hf in nuclear reactors, and Mg in automotive applications, often involves the co-activation of multiple deformation modes at the microscale. This imposes difficulties not only in the processing of these materials, but also in understanding and predicting their performance. Generally, plastic deformation modes in this class of materials include dislocation glide on the basal, prismatic and pyramidal planes as well as twinning [7]. ⟨*a*⟩ prismatic slip in Hf has been observed experimentally [8], and the critical resolved shear stress (CRSS) was measured at ~20 MPa at room temperature [9]. While no evidence of basal slip has been observed in experimental tests on single crystal Hf to our best knowledge, basal dislocations were observed in tests on polycrystalline specimens [10–12] and computational work has predicted it to be the preferred deformation mode [13]. Basal slip could play an important role in the mechanical performance of Hf, in a similar way to that in other HCP metals with close *c*/*a* ratios such as Ti [14,15] and Zr [16]. It could also have implications for hydride embrittlement of Hf control rods in hot water during operation, since hydride formation in some HCP metals, such as Zr, is achieved through partial dislocation glide on basal planes [17–20].

Being able to accurately predict the mechanical performance of materials in-service essentially relies on the knowledge of their fundamental mechanical behaviour and properties such as CRSS. Activating targeted slip systems in materials, and measuring their CRSS, require testing single crystal specimens with known crystal orientations under a well-defined stress state. This can be achieved through micromechanical testing as we showed previously on metallic [21–24] and ceramic [25,26] materials. Here we employ this approach to investigate:

1) the relative ease of basal *vs.* prismatic slip in Hf;

* Corresponding author.
E-mail address: siyang.wang15@imperial.ac.uk (S. Wang).

https://doi.org/10.1016/j.mtla.2024.102122
Received 3 May 2024; Accepted 10 May 2024
Available online 10 May 2024

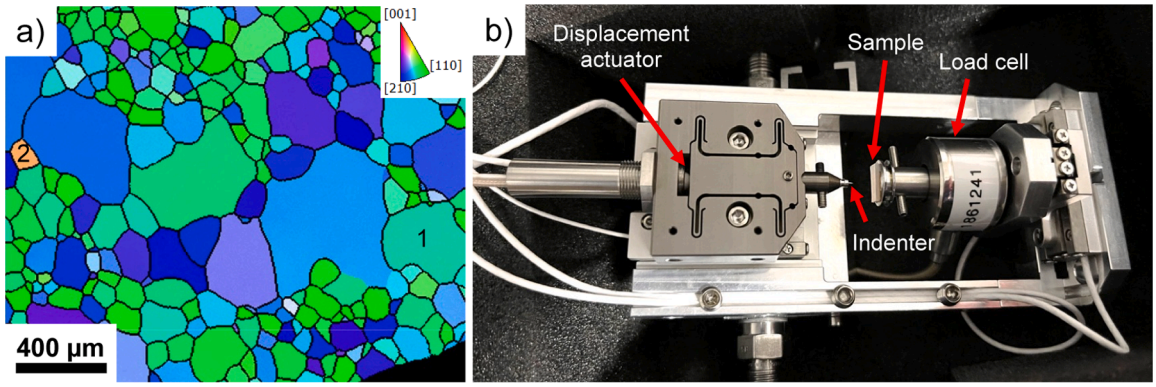

Fig. 1. (a) EBSD IPF-*z* map (*z*-axis points out of the page) of the material showing the as-annealed microstructure. The grains selected for activating prismatic slip (Grain 1) and basal slip (Grain 2) are indicated. (b) The Alemnis nanoindentation system used for *in situ* micropillar compression tests.

Table 1
The highest Schmid factors for all potential slip systems of the micropillars under the applied stress.

	⟨*a*⟩ prismatic	⟨*a*⟩ basal	⟨*a*⟩ pyramidal	First order ⟨*c* + *a*⟩ pyramidal	Second order ⟨*c* + *a*⟩ pyramidal
Grain 1	0.50	0.02	0.44	0.45	0.43
Grain 2	0.26	0.49	0.38	0.37	0.26

2) the CRSS for basal slip, if it does exist;
3) the slip and dislocation behaviour for these two slip systems.

The material studied in this work was cut from a drawn Hf alloy rod supplied commercially by Goodfellow Cambridge Ltd., and the chemical composition and mechanical properties provided are given in Tables S1 and S2. The samples were annealed at 1000 °C for 10 days in Ar atmosphere to promote recrystallisation and grain growth (akin to the annealing of Zr [27]), thereby forming large equiaxed grains (Fig. 1(a)). They were then mechanically ground with SiC abrasive papers, polished with colloidal silica, and finally electropolished in 10 vol.% perchloric acid (in methanol) at −50 °C for 90 s under an applied voltage of 30 V for analysis with electron backscatter diffraction (EBSD) and *in situ* scanning electron microscope (SEM) testing.

We used EBSD to reveal the crystal orientations of the grains, so as to select appropriate ones for activating targeted slip systems during subsequent micropillar compression tests. EBSD scanning was carried out on a Thermo Fisher Scientific (TFS) Quanta 650 SEM equipped with a Bruker eFlashHR (v2) EBSD camera, using a beam voltage of 20 kV and a probe current of ~10 nA.

Micropillar specimens (height = ~15 μm, mid-height diameter = ~5 μm, taper angle = ~2.5°) were fabricated in two grains showing high Schmid factors for prismatic (Grain 1 in Fig. 1(a)) and basal slip (Grain 2 in Fig. 1(a)) respectively, assuming a uniaxial load perpendicular to the sample surface. While the aspect ratio of the pillars should not affect the measured strength values for ductile (or non-defect-controlled) materials, it could affect the shape stability of the samples during the tests. Here, the aspect ratio was selected for consistency with our prior work [23,24] where stability was achieved. A detailed investigation into its effect on the deformation behaviour can be found in ref. [28]. For the two grains selected, the highest Schmid factors for all potential slip systems of the micropillars under the applied stress are listed in Table 1. Micropillars were fabricated *via* FIB milling on a TFS Helios 5 CX DualBeam microscope, using a FIB acceleration voltage of 30 kV. TFS Nanobuilder software was employed to automate the milling process. Three micropillars were made and tested in each grain. *In situ* SEM micropillar compression tests were conducted using a

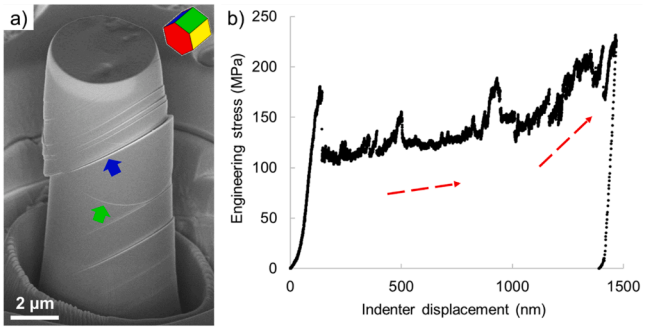

Fig. 2. (a) Post-deformation SEM image of a micropillar in Grain 1 showing ⟨*a*⟩ prismatic slip, with an insert of unit cell representation of the crystal orientation, oriented with respect to the viewing angle. (b) Mechanical response ((stress-displacement curve) of the pillar in (a) recorded during the test.

displacement-controlled Alemnis nanoindenter (Fig. 1(b)) on the Quanta 650 SEM. The pillars were deformed with a 10 μm-diameter indenter tip to achieve a uniaxial stress state for the tests. The loading speed was 5 nm/s, which corresponds to a nominal strain rate of $3.3 \times 10^{-4}\ s^{-1}$. During the tests, there might be radial friction forces between the indenter tip and the pillar top surface, which was found to be beneficial for the shape stability of the pillars [28].

When the *in situ* micropillar compression tests were complete, some electron transparent specimens were extracted from the deformed pillars for analysis with a transmission electron microscope (TEM), in order to gain insight into the fine structure of deformation features. This was achieved following the FIB lift-out procedure described in detail by Giannuzzi et al. [29], on a TFS Helios 5 Hydra CX DualBeam microscope. TEM and scanning TEM (STEM) imaging of the samples was conducted on a JEOL JEM-2100F TEM equipped with a Gatan 963.J453PTNS STEM detector using an acceleration voltage of 200 kV.

The mechanical behaviour of a micropillar showing high Schmid factor for one of the prismatic slip systems (0.50, "Grain 1″ in Table 1) is shown in Fig. 2. All the three pillars tested in this grain showed similar deformation behaviour, and a video recorded during one test is provided in Video S1. The stress-displacement curves for all the six micropillars tested are given in Figure S1. During plastic deformation, the applied strain was initially accommodated by activation of the prismatic slip system with the highest Schmid factor (the blue-coloured crystallographic plane in the unit cell overlaid on Fig. 2(a) and the ⟨*a*⟩ direction within it), as evidenced by the discrete slip bands on the pillar (one of the slip bands in this group is marked with the blue arrow in the image) parallel to the blue-coloured plane. Later in the plastic regime (when displacement reaches ~1000 nm), the activation of a second prismatic slip system can be observed (the slip band marked with the green arrow

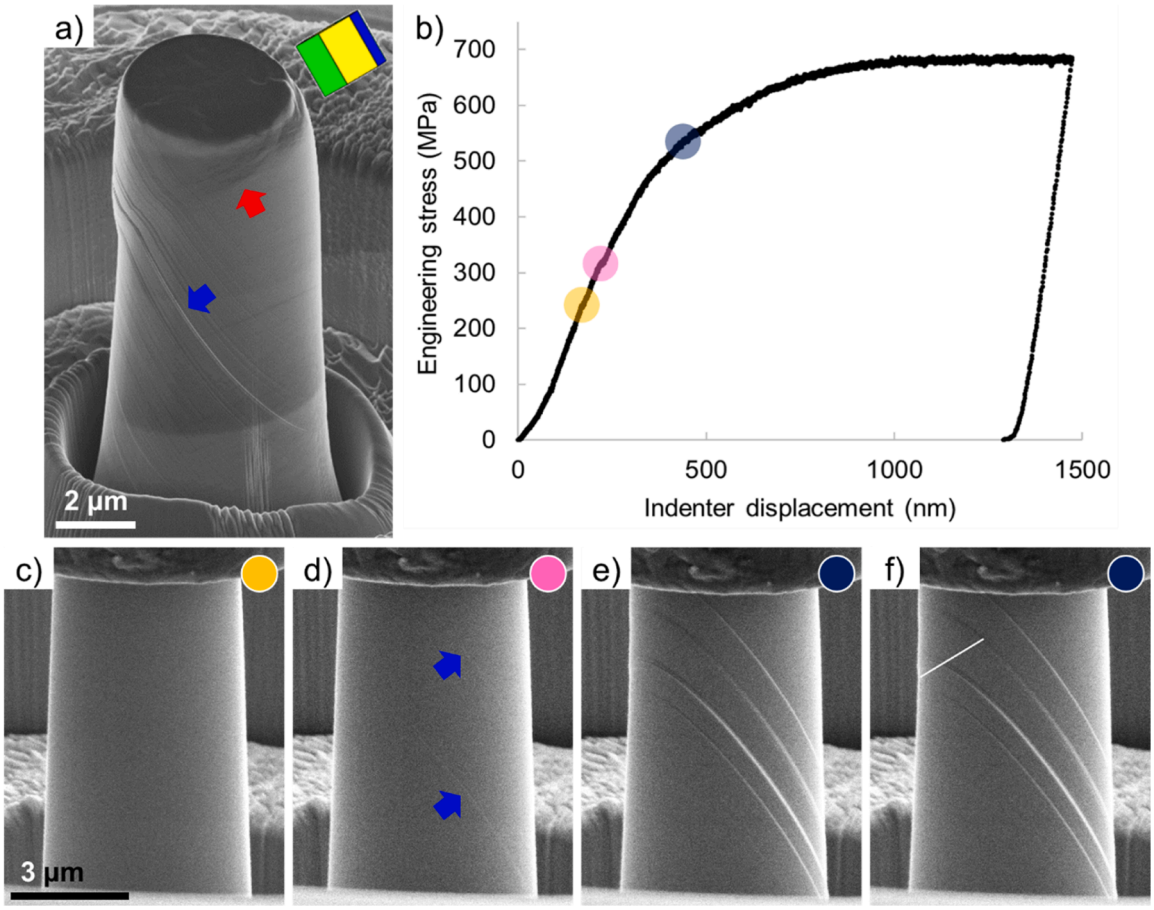

Fig. 3. (a) Post-deformation SEM image of a micropillar in Grain 2 showing both ⟨*a*⟩ prismatic and ⟨*a*⟩ basal slip, with an insert of unit cell representation of the crystal orientation, oriented with respect to the viewing angle. An image of the same pillar viewed from its left is given in Figure S2. (b) Mechanical response (stress-displacement curve) of the pillar in (a) recorded during the test. (c,d,e) Frames of the video recorded during the *in situ* test, taken at the points labelled on the stress-displacement curve in (b). The slip band parallel to the basal plane in (e) is highlighted in (f).

and those parallel to it, which are parallel to the green-coloured prismatic plane in the unit cell). Upon activation of the second slip system, an increase in work hardening rate occurred, as highlighted with the arrows on the stress-displacement curve in Fig. 2(b). The hardening rates are observed on the engineering stress-displacement (rather than true stress-strain) response, and we note that care must be taken in interpretation due to the taper of the micropillars and the strain localisation at the slip bands. For textured polycrystalline Hf compressed perpendicular to the *c*-axis where deformation was accommodated mainly by prismatic slip, a similar hardening behaviour (low work hardening rate at low strains and increased hardening rate at higher strains as the dislocations became tangled) was observed [12].

Generally, prismatic slip in Hf appears to be highly planar according to the post-deformation SEM image, which likely contributed to the stress drops on the stress-displacement curve as the dislocations move out of the pillar. This is similar to the behaviour of prismatic slip in Ti and Zr (planar slip and stress drops) [15,23,30], although the stress drops here in Hf are much less significant than those in Zr micropillars in our prior work [23]. This implies the existence of a resistance to rapid dislocation motion or source activation in the alloy studied, potentially induced by the Zr substitutional and/or O interstitial atoms. Note that the large stress drop of ~70 MPa soon after yielding in Fig. 2(b) was not reproduced on all the stress-displacement curves for the pillars in this grain (Figure S1), indicating that it is unlikely caused by a systematic artefact such as a FIB-induced surface damage layer (*i.e.*, its origin is unlikely different to that of the stress drops later in the plastic regime as we discussed above).

For the three pillars tested, the CRSS values for prismatic slip were calculated to be 61 MPa, 66 MPa and 63 MPa respectively. These are evidently higher than that measured by Das and Mitchell (~20 MPa [9]) using larger scale specimens, which could be a result of different alloy compositions and/or specimen sizes. Specifically, the alloy we used nominally contains 2.8 wt.% Zr and 150 ppm O (Table S1). The O content is comparable to that in the alloy that Das and Mitchell used (160 ppm), while the Zr content is nearly twice theirs (1.41 wt.% in their material). The Zr atoms may introduce a more pronounced substitutional solid solution hardening in the material we studied, leading to higher measured CRSS. The size effect in small scale mechanical testing could also give rise to elevated strength values [31]. However, this effect is often insignificant in micropillars of over a few microns in size [24,32]. In our prior work [24], CRSS values extracted from tests on 5-μm pillars in Zr were found comparable to size-independent values that had been proved suitable for crystal plasticity modelling of plastic flow in a macroscopic textured polycrystal [16].

Fig. 3 illustrates the deformation behaviour of a micropillar in Grain 2 which showed a high Schmid factor for basal slip (Table 1). Two intersecting sets of slip bands can be observed on the post-deformation image in Fig. 3(a): one parallel to the blue-coloured prismatic plane in the unit cell (marked with the blue arrow) and one parallel to the basal plane (marked with the red arrow). For the latter, the slip band appears to be broad and diffuse. An image of the same pillar viewed from its left is given in Figure S2.

The video recorded during the test (Video S2) was examined to work out which slip system was activated first. Some frames are shown in

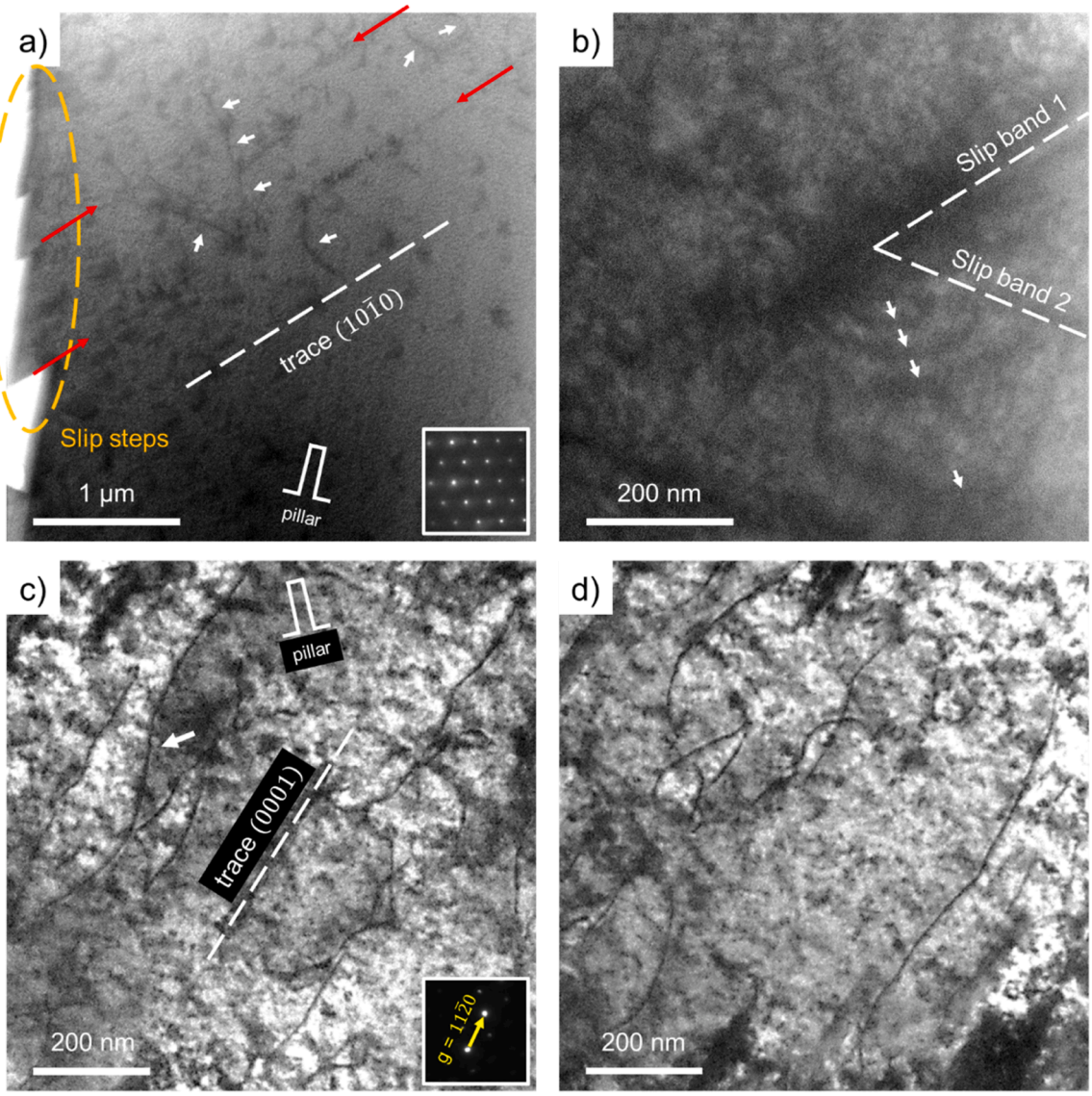

Fig. 4. TEM images of thin foil specimens lifted out from deformed micropillars in (a,b) Grain 1 and (c,d) Grain 2. (a) is a STEM image, while (b,c,d) are TEM images. All images are bright-field. The serrations on the left of (a) are slip steps on the side surface of the pillar. The orientations of the images with respect to the original micropillars for (a) and (b) are sketched in (a), and for (c) and (d) sketched in (c). The zone axes / diffraction vectors are the same for (a) and (b) (on [0001] zone, shown in (a)), and the same for (c) and (d) ($g = 11\bar{2}0$, shown in (c)).

Fig. 3(c-f), which were taken at the corresponding points labelled on the stress-displacement curve in (b). No apparent slip band was detected on the pillar surface upon yield (Fig. 3(c)). Shortly afterwards, two slip bands parallel to the prismatic plane formed (Fig. 3(d)). Evidence of basal slip was not observed until the point of Fig. 3(e), where a slip band parallel to the basal plane - highlighted in Fig. 3(f) - appeared. It is thus clear that prismatic slip occurred prior to basal slip on this pillar during deformation, *i.e.*, the pillar yielded by virtue of prismatic slip. This is supported by the fact that the resolved shear stress on the activated prismatic slip system upon yield is 63 MPa, which agrees well with the CRSS for prismatic slip extracted earlier with the pillars in Grain 1. The "absence" of plastic deformation feature in Fig. 3(c) could be a result of a) dislocation nucleation in the pillar interior, b) technique/microscope/condition not sufficient for detecting very subtle deformation or c) slip band formation on the rear side of the pillar.

It is therefore challenging to determine the CRSS for basal slip unambiguously, owing to the difficulty in accurately locating the point where it initiated. This should be a general problem for HCP materials whose CRSS for basal slip is over ~twice that for prismatic slip, as in uniaxial tests it is geometrically impossible to have a crystal simultaneously showing high Schmid factor (near 0.5) for basal slip and low Schmid factor ($\ll 0.2$) for prismatic slip [23]. Only a range can be given instead: the lower and upper bounds are the resolved shear stresses on the $\langle a \rangle$ basal slip system with the highest Schmid factor at the yield point and at the point where basal slip was first observed (*i.e.*, the yellow and the dark blue dots on the curve in Fig. 3(b)), respectively. Averaging over the results for the three pillars tested gives a lower bound of ~150 MPa and an upper bound of ~250 MPa. The high CRSS for basal slip, and hence the difficulty in activating it (which requires aligning the crystal nearly perfectly as we showed), could be the reason for the fact that previously basal slip was never observed in single crystal tests [2] and only occasionally in polycrystal tests [10–12]. For example, in ref. [12], compression perpendicular to the *c*-axis (for textured polycrystals) triggered prismatic slip and twinning, while compression along the *c*-axis was accommodated mainly by pyramidal slip. Basal dislocations were only observed within some of the twins, where abrupt changes in orientation could make local stress states favourable for basal slip.

We have activated the targeted slip systems (the $\langle a \rangle$ prismatic and

the ⟨a⟩ basal for pillars in Grains 1 and 2, respectively) in the compression tests. Here we term these two slip systems as the respective "major slip system" for the two sets of pillars. The TEM specimens were lifted out such that the slip plane of the major slip system is perpendicular to the foil plane, and the slip direction (hence Burgers vector of relevant dislocations) is parallel to the foil plane, Figure S3.

The dislocation structure in a tested pillar in Grain 1 is shown in Fig. 4(a). In general, the sample appears to be relatively "clean" presumably due to a) the small amount of deformation imposed, b) the lack of lateral constraint for the test geometry and c) the highly planar nature of prismatic slip, hence the dislocations had left the sample. For example, the biggest slip step in the image (~400 nm wide) suggests that over 1000 dislocations had moved out of the pillar along that plane. Screw dislocations are observed aligned along the slip bands (parallel to the trace of the $(10\bar{1}0)$ plane and marked with the red arrows). We note that, as the electron beam is parallel to the prismatic planes, the apparent straightness of these dislocations along the slip bands in the image does not necessarily indicate straightness within the slip plane.

There are also some curved dislocations in the image (marked with the white arrows). Given that the prismatic planes are all perpendicular to the image plane and the basal plane was under negligible stress during the test (Table 1), these curved segments could either be pre-existing dislocations or ⟨a⟩ dislocations cross-slipped onto the pyramidal plane (s). Notably, the two ⟨a⟩ pyramidal slip systems that share the ⟨a⟩ direction with the major prismatic slip system exhibit the highest Schmid factors (0.44 and 0.43) within their family, indicating the presence of potentially sufficient stress for cross-slipping.

Fig. 4(b) shows the microstructure of a local area where two slip bands (for the two activated prismatic slip systems) intersected forming a Frank-Read source, from which at least four dislocations (marked with the arrows) were emitted. This is consistent with the classic "stage II" of single crystal deformation, where a second slip system is activated giving rise to forest hardening (Fig. 2(b), the increase in hardening rate when displacement > ~1000 nm).

The dislocation structure in a tested pillar in Grain 2 is shown in Fig. 4(c,d). The diffraction vector was selected (through tilting the sample about the *c*-axis of the crystal) to maximise the visibility of dislocations gliding on the basal plane. Although the screw dislocations were broadly aligned with the trace of (0001) plane, they were rarely straight and typically contained curved segments bowed out from the basal plane (such as the one marked with the arrow in Fig. 4(c)), indicating intensive cross-slip. This is consistent with the broad and diffuse character of the slip bands (Fig. 3(a)), and the behaviour of basal slip in Zr and Ti where it is never planar [15,24,30]. The origin of such intensive cross-slip could be a kink-pair mechanism where screw dislocations extend on the prismatic plane as they glide on the basal plane [30]. Akhtar [33] also attributed the wavy nature of basal slip in Zr and Ti to cross-slip onto the prismatic plane where dissociation into partials is more favoured, and suggested that this might be related to the relative ease of basal and prismatic slip. Nonetheless, the origin of such anisotropic slip behaviour in HCP metals remains unclear despite many decades of research indicating its complicated nature, which likely involves the effects of Peierls stresses, stacking fault energies and other strengthening mechanisms. It is also worth noting that, for both sets of samples, no evidence of deformation twinning was observed.

In summary, we studied the behaviour of prismatic and basal slip in a Hf alloy using *in situ* SEM compression tests of micropillars with selected crystal orientations. Prismatic slip is generally highly planar, and the CRSS is ~63 MPa. Upon activation of multiple prismatic slip systems, blocked slip bands by one another act as Frank-Read sources giving rise to forest hardening. Basal slip involves intensive cross-slip. Its CRSS cannot be unambiguously determined, as it initiated after prismatic slip even for the most favourable orientation. Through examination of *in situ* data, the CRSS for basal slip is estimated to be 150–250 MPa. In general, the characters of these two slip systems in Hf resemble those in Zr and Ti, where prismatic slip is planar and basal slip is wavy. The $CRSS_{basal}$ to $CRSS_{prismatic}$ ratio for Hf is higher than those for Zr (~1.3 [16,23]) and Ti (~1.15 [15]) likely tied to its lower *c/a* ratio [7]. The fundamental properties and behaviour of these two slip systems we report here enable the modelling of processes such as polycrystal deformation, hydride formation (potentially through the approach used by Kolesnik et al. on Zr [19]), or the two combined, for further understanding and/or predicting degradation of Hf alloy control rods. Furthermore, our results on Hf, when compared with those on Ti and Zr, imply a similarity in the qualitative behaviour of the studied slip systems while a quantitative difference in the relative ease for their activation. The origin of these could be further explored experimentally and computationally for better understanding the general principle of the micromechanics of HCP alloys, thereby ensuring their long-term structural integrity in-service.

CRediT authorship contribution statement

Siyang Wang: Writing – review & editing, Writing – original draft, Visualization, Validation, Methodology, Investigation, Formal analysis, Data curation, Conceptualization. **Di Wang:** Writing – review & editing, Visualization, Validation, Investigation, Formal analysis, Data curation.

Declaration of competing interest

The authors declare that they have no known competing financial interests or personal relationships that could have appeared to influence the work reported in this paper.

Acknowledgements

We thank Prof Finn Giuliani for proofreading the manuscript. SW acknowledges Imperial College London for funding his Imperial College Research Fellowship. The TFS Quanta SEM used was supported by the Shell AIMS UTC and is housed in the Harvey Flower EM suite at Imperial College London. The TFS dual beam microscopes used is part of the cryo-EPS facility at Imperial College London funded by Engineering and Physical Sciences Research Council (EP/V007661/1). The Matlab code used to calculate Schmid factors and plot unit cells for representation of crystal orientations was written by Dr Vivian Tong currently at National Physical Laboratory UK.

Supplementary materials

Supplementary material associated with this article can be found, in the online version, at doi:10.1016/j.mtla.2024.102122.

References

[1] D.S. Eppelsheimer, D.S. Gould, Deformation characteristics of hafnium, Nature 177 (1956) 241–242, https://doi.org/10.1038/177241b0.
[2] G. Das, T.E. Mitchell, Mechanical properties of hafnium single crystals, Metallurgical Transactions 4 (1973) 1405–1413, https://doi.org/10.1007/BF02644539.
[3] J. Schemel, ASTM Manual on Zirconium and Hafnium, ASTM International100 Barr Harbor Drive, PO Box C700, West Conshohocken, PA 19428-2959, 1977. https://doi.org/10.1520/STP639-EB.
[4] S. Wang, F. Giuliani, T.Ben Britton, Microstructure and formation mechanisms of δ-hydrides in variable grain size Zircaloy-4 studied by electron backscatter diffraction, Acta Mater. 169 (2019) 76–87, https://doi.org/10.1016/J.ACTAMAT.2019.02.042.
[5] H.W. Keller, J.M. Shallenberger, D.A. Hollein, A.C. Hott, Development of hafnium and comparison with other pressurized water reactor control rod materials, Nucl. Technol. 59 (1982) 476–482, https://doi.org/10.13182/NT82-A33005.
[6] S. Yadav, K.T. Ramesh, The mechanical behavior of polycrystalline hafnium: Strain-rate and temperature dependence, Materials Science and Engineering A 246 (1998) 265–281, https://doi.org/10.1016/s0921-5093(97)00746-6.
[7] T.B. Britton, F.P.E. Dunne, A.J. Wilkinson, On the mechanistic basis of deformation at the microscale in hexagonal close-packed metals, Proceedings of the Royal Society A: Mathematical, Physical and Engineering Sciences 471 (2015) 20140881, https://doi.org/10.1098/rspa.2014.0881.

[8] F.W. Vahldiek, Hafnium I. Microstructure, Journal of The Less-Common Metals 19 (1969) 83–92, https://doi.org/10.1016/0022-5088(69)90023-X.
[9] G. Das, T.E. Mitchell, Mechanical properties of hafnium single crystals, Metallurgical Transactions 4 (1973) 1405–1413, https://doi.org/10.1007/BF02644539.
[10] R.L. Straw, N.S. Stoloff, The effects of oxygen on deformation and fracture of polycrystalline hafnium, Metallurgical Transactions A 7 (1976) 312–314, https://doi.org/10.1007/BF02644476.
[11] S.M. Seelinger, N.S. Stoloff, The effect of hydrogen on deformation and fracture processes in hafnium, Metallurgical Transactions 2 (1971) 1481–1484, https://doi.org/10.1007/BF02913384.
[12] E. Cerreta, G.T. Gray, The influence of texture, strain rate, temperature, and chemistry on the mechanical behavior of hafnium, Metallurgical and Materials Transactions A 35 (2004) 1999–2011, https://doi.org/10.1007/s11661-004-0149-x.
[13] H.Y. Zhu, X.F. He, Z.R. Liu, The preferred slip plane of nuclear material of Hafnium: A first-principles study, Comput. Mater. Sci. 157 (2019) 25–30, https://doi.org/10.1016/j.commatsci.2018.10.030.
[14] Z. Zhang, T.S. Jun, T.B. Britton, F.P.E. Dunne, Intrinsic anisotropy of strain rate sensitivity in single crystal alpha titanium, Acta Mater. 118 (2016) 317–330, https://doi.org/10.1016/j.actamat.2016.07.044.
[15] J. Gong, A.J. Wilkinson, Anisotropy in the plastic flow properties of single-crystal α titanium determined from micro-cantilever beams, Acta Mater. 57 (2009) 5693–5705, https://doi.org/10.1016/j.actamat.2009.07.064.
[16] J. Gong, T. Benjamin Britton, M.A. Cuddihy, F.P.E. Dunne, A.J. Wilkinson, <a>Prismatic, <a>basal, and <c+a>slip strengths of commercially pure Zr by micro-cantilever tests, Acta Mater. 96 (2015) 249–257, https://doi.org/10.1016/j.actamat.2015.06.020.
[17] G.J.C. Carpenter, The precipitation of γ-zirconium hydride in zirconium, Acta Metallurgica 26 (1978) 1225–1235, https://doi.org/10.1016/0001-6160(78)90006-8.
[18] G.C. Weatherly, The precipitation of γ-hydride plates in zirconium, Acta Metallurgica 29 (1980) 501, https://doi.org/10.1016/0001-6160(81)90074-2.
[19] M. Kolesnik, T. Aliev, V. Likhanskii, The modeling of the hydrogen solid solubility hysteresis in zirconium alloys, Acta Mater. 177 (2019) 131–140, https://doi.org/10.1016/j.actamat.2019.07.044.
[20] S. Wang, On the origin of the hydride precipitation-dissolution hysteresis in zirconium: Comments on Short Communication of G.A. McRae and C.E. Coleman published in Journal of Nuclear Materials 568 (2022) 153889, Journal of Nuclear Materials 570 (2022) 153952, https://doi.org/10.1016/j.jnucmat.2022.153952.
[21] S. Wang, S. Kalácska, X. Maeder, J. Michler, F. Giuliani, T.Ben Britton, The effect of δ-hydride on the micromechanical deformation of a Zr alloy studied by in situ high angular resolution electron backscatter diffraction, Scr. Mater. 173 (2019) 101–105, https://doi.org/10.1016/j.scriptamat.2019.08.006.
[22] S. Wang, O. Gavalda-Diaz, T. Luo, L. Guo, E. Lovell, N. Wilson, B. Gault, M.P. Ryan, F. Giuliani, The effect of hydrogen on the multiscale mechanical behaviour of a La(Fe,Mn,Si)13-based magnetocaloric material, J. Alloys. Compd. 906 (2022) 164274, https://doi.org/10.1016/j.jallcom.2022.164274.
[23] S. Wang, F. Giuliani, T. Ben Britton, Slip–hydride interactions in Zircaloy-4: Multiscale mechanical testing and characterisation, Acta Mater. 200 (2020) 537–550, https://doi.org/10.1016/j.actamat.2020.09.038.
[24] S. Wang, F. Giuliani, T.Ben Britton, Variable temperature micropillar compression to reveal <a>basal slip properties of Zircaloy-4, Scr. Mater. 162 (2019) 451–455, https://doi.org/10.1016/j.scriptamat.2018.12.014.
[25] S. Wang, Z. Shen, A. Omirkhan, O. Gavalda-diaz, M.P. Ryan, F. Giuliani, Determining the fundamental failure modes in Ni-rich lithium ion battery cathodes, J. Eur. Ceram. Soc. 43 (2023) 7553–7560, https://doi.org/10.1016/j.jeurceramsoc.2023.08.021.
[26] S. Wang, O. Gavalda-Diaz, J. Lyons, F. Giuliani, Shear and delamination behaviour of basal planes in Zr3AlC2 MAX phase studied by micromechanical testing, Scr. Mater. 240 (2024) 115829, https://doi.org/10.1016/j.scriptamat.2023.115829.
[27] V. Tong, B. Britton, Formation of very large 'blocky alpha' grains in Zircaloy-4, Acta Mater. 129 (2017) 510–520, https://doi.org/10.1016/j.actamat.2017.03.002.
[28] D. Raabe, D. Ma, F. Roters, Effects of initial orientation, sample geometry and friction on anisotropy and crystallographic orientation changes in single crystal microcompression deformation: A crystal plasticity finite element study, Acta Mater. 55 (2007) 4567–4583, https://doi.org/10.1016/j.actamat.2007.04.023.
[29] L.A. Giannuzzi, J.L. Drown, S.R. Brown, R.B. Irwin, F.A. Stevie, Applications of the FIB lift-out technique for TEM specimen preparation, Microsc. Res. Tech. 41 (1998) 285–290, https://doi.org/10.1002/(SICI)1097-0029(19980515)41:4<285::AID-JEMT1>3.0.CO;2-Q.
[30] D. Caillard, M. Gaumé, F. Onimus, Glide and cross-slip of a-dislocations in Zr and Ti, Acta Mater. 155 (2018) 23–34, https://doi.org/10.1016/j.actamat.2018.05.038.
[31] Q. Sun, Q. Guo, X. Yao, L. Xiao, J.R. Greer, J. Sun, Size effects in strength and plasticity of single-crystalline titanium micropillars with prismatic slip orientation, Scr. Mater. 65 (2011) 473–476, https://doi.org/10.1016/j.scriptamat.2011.05.033.
[32] O. Torrents Abad, J.M. Wheeler, J. Michler, A.S. Schneider, E. Arzt, Temperature-dependent size effects on the strength of Ta and W micropillars, Acta Mater. 103 (2016) 483–494, https://doi.org/10.1016/j.actamat.2015.10.016.
[33] A. Akhtar, Basal slip and twinning in α-titanium single crystals, Metallurgical Transactions A 6 (1975) 1105–1113, https://doi.org/10.1007/BF02661366.